PHYSICAL REVIEW B **96**, 155202 (2017)

Terahertz surface emission of *d*-band electrons from a layered tungsten disulfide crystal by the surface field

Longhui Zhang, Yuanyuan Huang, Qiyi Zhao, Lipeng Zhu, Zehan Yao, Yixuan Zhou, Wanyi Du, and Xinlong Xu[*]
Shaanxi Joint Lab of Graphene, State Key Lab Incubation Base of Photoelectric Technology and Functional Materials,
International Collaborative Center on Photoelectric Technology and Nano Functional Materials,
Institute of Photonics & Photon-Technology, Northwest University, Xi'an 710069, China

(Received 3 July 2017; revised manuscript received 14 September 2017; published 6 October 2017)

Terahertz (THz) time-domain emission spectroscopy in both transmission and reflection configurations has been employed to understand the THz radiation property and surface properties of tungsten disulfide (WS_2). We observed only one polarization of THz radiation under different polarization of pump beam and a saturation effect with the increasing of pump power. The results are different from that of MoS_2 based on optical rectification in spite of similar physical and optoelectronic properties of them. The nonlinear optical coefficient calculation based on first-principle method combined with the azimuthal angle dependence of THz radiation implies that THz radiation is insensitive to the azimuthal angle in WS_2. From the pump polarization angle dependence of THz radiation, we find that the contribution due to the nonlinear effect is only 12% approximately. All these suggest the main THz mechanism from WS_2 is due to the surface depletion field induced by the surface states. We also analyzed the surface field features of WS_2 with the maximum surface depletion field of approximate 1.2×10^5 V/cm. Fresnel law combined with the dipole radiation model is also used to analyze the angular dependence of THz radiation. The results can not only afford a fundamental THz radiation property of layered materials, but also promote the development of THz devices based on layered materials.

DOI: 10.1103/PhysRevB.96.155202

I. INTRODUCTION

Layered materials are a kind of advanced materials, which demonstrate rich physics such as topological order [1], room-temperature quantum Hall effect [2], superconducting order [3], magnetic order [4], and so on. Layered transition-metal dichalcogenides (TMDCs) such as MoS_2, WS_2, etc., are these kinds of materials, which have remarkable optical properties such as polarization-dependent optical absorption [5], indirect-to-direct transition with layers [6], saturable absorption [7], valley-dependent photoluminence [8], as well as enhanced nonlinear optics response [9]. These optical properties make TMDCs suitable for the next generation of optoelectronics in light-emitting diodes [10], solar cell [11], field-effect transistor [12], and photodetector [13]. Unlike gapless graphene, TMDCs demonstrate a tunable band gap in the visible region, which improves the on/off ratio in optoelectronic devices. They also demonstrate ultrafast carrier dynamics [14] in the ps scale [15], which suggests that TMDCs are promising for high-speed optoelectronic devices up to terahertz (THz) frequency.

The THz region viewed as a gap between photonics and electronics has some unique properties such as low photon energy, nonpolar substance penetrability, fingerprinting characterization of biochemical molecules, and so on. It presents vast applications in security [16], medical imaging [17], and high-speed communication [18]. Recently, the research on THz properties of TMDCs is blooming from foundation for the THz photonics. With the development of THz technology and layered materials science, two general treads are in progress, one for the property understanding of layered materials with THz technology and one for THz applications based on layered materials. Docherty *et al.* studied THz conductivity of MoS_2 and WSe_2 [15] and they attributed the ultrafast photoconductivity responses to the charge trapping at surface states. Deng *et al.* investigated ultrahigh transmission of monolayer MoS_2 with different carrier concentration in THz region theoretically [19]. Recently, our group has analyzed the dielectric property of MoS_2 ranging from THz to visible regions [20] as well as its THz radiation mechanism based on dominant optical rectification [21]. However, few THz data have been reported for the tungsten disulfide (WS_2). WS_2 is similar to MoS_2 with typical *X*-*M*-*X* (where *X* is the sulfur and *M* is the tungsten or molybdenum) sandwich structure and stacked by van der Waals interaction. The bulk WS_2 is an indirect semiconductor with the band gap energy $E_g = 1.35$ eV, which is quite close to MoS_2 with $E_g = 1.29$ eV. Both of them belong to hexagonal symmetry and have similar excellent optoelectronic properties. THz generation from WS_2 directly under a femtosecond laser is less reported, as is the difference of THz radiation mechanisms between WS_2 and MoS_2.

Unlike the traditional THz time-domain transmission/reflection spectroscopy, THz surface emission spectroscopy under transmission and reflection configuration provide an ideal platform for the surface research on the optoelectronic semiconductors and make up for the limitation of surface research with THz technology effectively. This tool can be used to study the THz radiation and surface properties of the materials. THz radiation from the surface of semiconductors carry out the information of amplitude, phase, polarity, polarization, etc., from which we can deduce the doping concentration, carrier mobility, the static field information, and so on [22]. THz surface emission spectroscopy has been mainly used for traditional III-V group semiconductors such as GaAs [23], InAs, and InSb [24], IV group semiconductors such as back silicon, and aligned carbon nanotubes [25], which are

---

[*] Corresponding author: xlxuphy@nwu.edu.cn

©2017 American Physical Society

mainly from the *p*-band electrons. However, TMDCs as a type of IVB-VIA group semiconductors, the *d*-band electrons play an important role in the electronic structure. The *p*-band and *d*-band electrons have different angular momentum quantum numbers, which is the basis for bond formation and their wave functions present a dumbbell and a four-petal shape respectively. Thus a full understanding of THz radiation properties from dominated *d*-band electrons in the layered materials is highly desirable. On the other side, TMDCs also have high electron mobility, fast recombination rates, and a short photoexcited carrier lifetime [26], which has potential applications in ultrafast broadband THz emitters.

In this work, THz emission spectroscopy system with both reflection and transmission configurations is used as a noncontact tool to investigate the THz radiation and surface properties from a layered 2H-WS_2 crystal under the linearly polarized femtosecond laser excitation effectively. The radiated THz amplitude demonstrated a saturation effect on the incident pump influence, which is mainly due to the screening effect of the surface depletion field from surface states. This is quite different from the THz generation mechanism in MoS_2, which is mainly based on the optical rectification as reported by our group [21]. THz radiation is also insensitive to the azimuthal angle of the sample with the radiation contribution from the nonlinear effect of approximate 12% at various polarization of the pump beam, which is also distinguished from that of MoS_2. This is consistent with the nonlinear optical coefficient calculation by the first-principle methods. These results suggest that the dominated THz radiation mechanism is from the electric field accelerating photocarriers by the surface field, which are different from that of MoS_2 in spite of similar physical and other optoelectronic properties between them. Besides, we analyzed the surface field characterization of WS_2 crystal and found the maximum value of the surface depletion field could be as high as 1.2×10^5 V/cm. The angular dependent THz radiation can be described by Fresnel law combined with the dipole radiation models, which suggests the high THz radiation at the Brewster angle. The results can not only afford a fundamental THz radiation property of WS_2 crystal, but also demonstrate potential photoconductive switch and THz emitters based on the WS_2 materials.

II. SAMPLE CHARACTERIZATION

The WS_2 crystal is a typical layered material by stacking S-W-S layer by layer with van der Waals interactions. In general, WS_2 has three polytype structures including hexagonal symmetry (2*H*-), rhombohedral symmetry (3*R*-), and tetragonal symmetry (1*T*-), which can be transformed into each other under different conditions [26]. The size of our free-standing sample (HQ graphene) is approximately $12 \times 12\,\text{mm}^2$ and 60 μm in thickness. The x-ray diffraction (XRD, HaoYuan Instrument) is employed to confirm the polytype of the WS_2. The set of diffraction peaks [Fig. 1(a)] labeled as (002), (004), (006), (008) arises from the reflections of crystal basal planes [27]. The peak positions and intensities correspond to the 2*H*-WS_2 phase (JCPDS:8-237) indicating that crystal WS_2 belongs to the 2*H*-polytype with the hexagonal space group $D_{6\text{h}}$. The Raman spectrum (model invia from Renishaw company) of the sample is measured under 514.5 nm excitation as shown in Fig. 1(b). Two primary characteristics the A_{1g} mode ($356.1\,\text{cm}^{-1}$) and the E_{2g} mode ($421.4\,\text{cm}^{-1}$), are the motion of W + S in the *x*-*y* plane and along the *z* axis respectively. This confirms that the WS_2 sample is a high-quality crystal sample. The small peaks observed at 172, 194, 232, 521, and $583\,\text{cm}^{-1}$ have been assigned to second-order Raman modes due to the phonon couplings with a nonzero momentum, respectively [28].

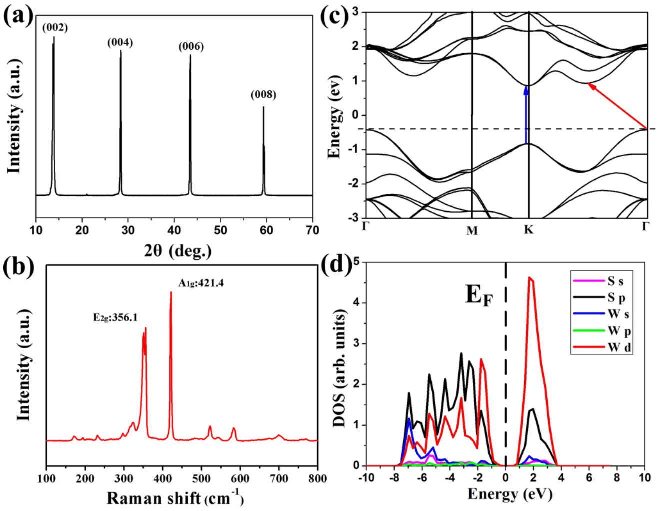

FIG. 1. Characterization of WS_2 crystal for (a) x-ray-diffraction spectrum; (b) Raman spectrum under 514.5 nm excitation; (c) simplified electric band structure. The blue and red arrows indicate the direct and indirect transitions from the valence to the conduction band, respectively. (d) Partial density of states of crystal WS_2.

The simplified electric-band structure of the bulk WS_2 is calculated from VASP (Vienna Ab-initio Simulation Package) with the lattice constants *a, c* and the internal coordinate *z* are 3.171, 12.359, and 3.095 Å, respectively. The band-gap transition takes place at the Γ point for indirect transition and at the *K* point for direct transition and are represented by blue and red arrows in Fig. 1(c) respectively. Figure 1(d) shows the partial densities of states corresponding to the electric band structures of WS_2. Obviously, the main contribution to the lower valence bands is from both the *p* state of the sulfur (S) atom and the *d* state of the tungsten (W) atom. The higher occupied valence bands are mainly occupied by the *d* state of the W atom.

III. RESULTS AND DISCUSSIONS

THz time-domain emission spectroscopy system with both reflection [Fig. 2(a)] and transmission [Fig. 2(b)] configurations are utilized to understand the THz radiation property of WS_2 at room temperature. The infrared laser (800 nm central wavelength) from a mode-locked Ti:sapphire regenerative amplifier (35 fs pulse duration and 1 KHz repetition rate) is divided into two beams by a beam splitter. The diameter of the pump beam to generate THz radiation is approximately 3 mm. In the reflection configuration, the pump beam is focused onto the surface of the sample at 45° incident angle. The THz radiation is collected via a pair of off-axis parabolic mirrors and then focused collinearly with the probe beam

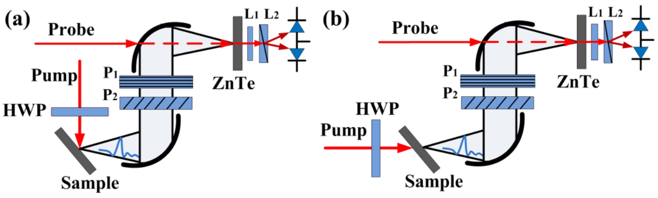

FIG. 2. Schematic of the reflection (a) and transmission (b) configurations of THz time-domain emission spectroscopy. HWP: half-wave plate, wire-grid polarizer P_1 and P_2 are perpendicular and 45° aligned; L_1 and L_2 are a quarter-wave plate and a Wollaston prism respectively.

to the zinc telluride [ZnTe (110)]. The probe beam passes through a quarter-wave plate and a Wollaston prism and then is detected by a pair of balanced diodes as shown in Fig. 2(a). In the transmission configuration, the pump pulse is adjusted to illuminate on the sample at different incident angles [Fig. 2(b)]. The half-wave plate (HWP) and wire-grid polarizer (WGP) in the optical path are used to adjust the polarization of the pump beam and the THz radiation, respectively.

When a femtosecond laser beam illuminates on the semiconductor surface, several generation mechanisms can result in THz radiation. In general, it is attributed to the ultrafast transient change of polarization and photocurrent generated by carriers, which can be described by

$$E_{\mathrm{THz}} \propto \frac{\partial P^2}{\partial t^2} + \frac{\partial J}{\partial t}, \qquad (1)$$

where P is the nonlinear polarization, which induces optical rectification based on nonlinear response [29–31]. J is the current density, which is induced by the photocarrier surging under the intrinsic or extrinsic electric field. As polarization is crystal symmetry dependent, the first term is usually azimuthal angle dependent with the sample symmetry. The second term demonstrates azimuthal angle independence but a polarity reverse of THz radiation pulses with different electric-field direction by the surface depletion field [32–34] or the polarity unreversed by the photo-Dember effect [35,36]. THz time-domain emission spectroscopy under transmission and reflection configurations provides an ideal platform for the studying of the dominated THz generation mechanism of $2H$-WS_2.

A. THz radiation under reflection configuration

In the reflection configuration, the polarization of the pump beam [X_P, Y_S in Fig. 3(a)] and the polarization of THz waves [E_X horizontal polarization, E_Y vertical polarization in Fig. 3(a)] can be taken by the half-wave plate and wire-grid polarizer as demonstrated in Fig. 3(a) with *XYZ* and *X'Y'Z'* representing the laboratory and crystals coordinate, respectively. The THz time-domain wave forms of two components under *P*- and *S*-polarized excitation are presented in Figs. 3(b) and 3(c) respectively. THz E_X components can hardly be affected by the polarized excitation with both *P*- and *S*-polarization excitation, while THz E_Y components are almost close to zero under different polarization excitation. This suggests that the dominant THz energy distributes along

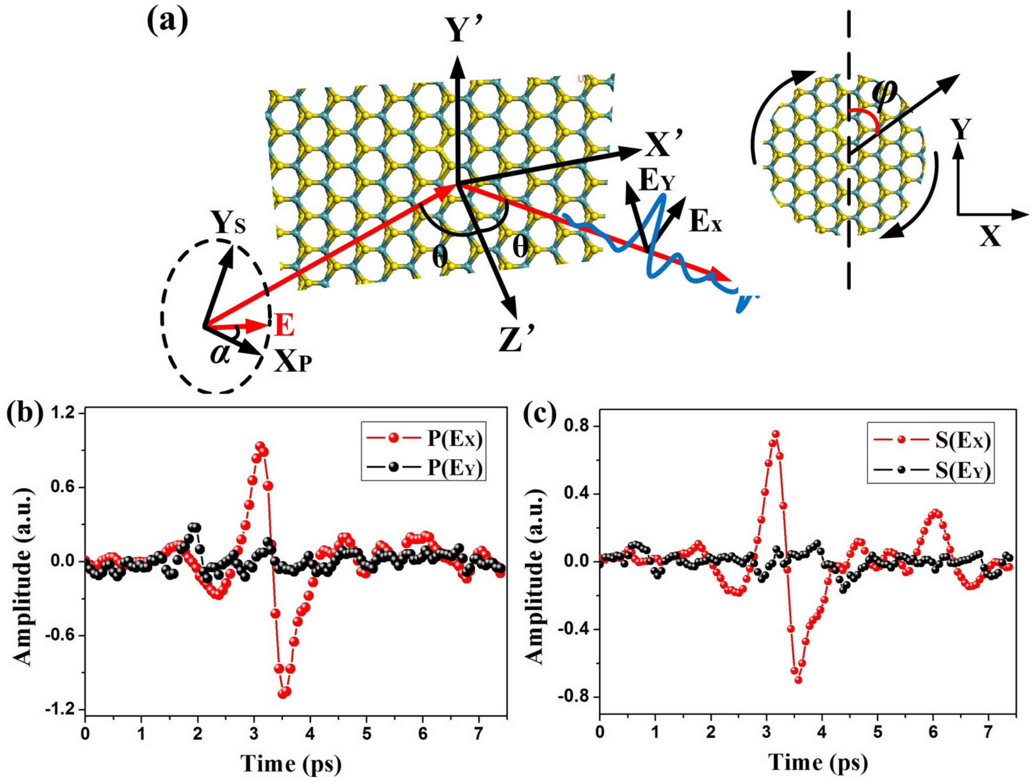

FIG. 3. (a) Schematic of THz generation under reflection configuration. *XYZ* and *X'Y'Z'* represent the laboratory and crystals coordinate, respectively and the inset presents the WS_2 geometry with azimuthal angle; *X* and *Y* components of generated THz electric field under (b) *P*-polarized and (c) *S*-polarized IR laser illuminations.

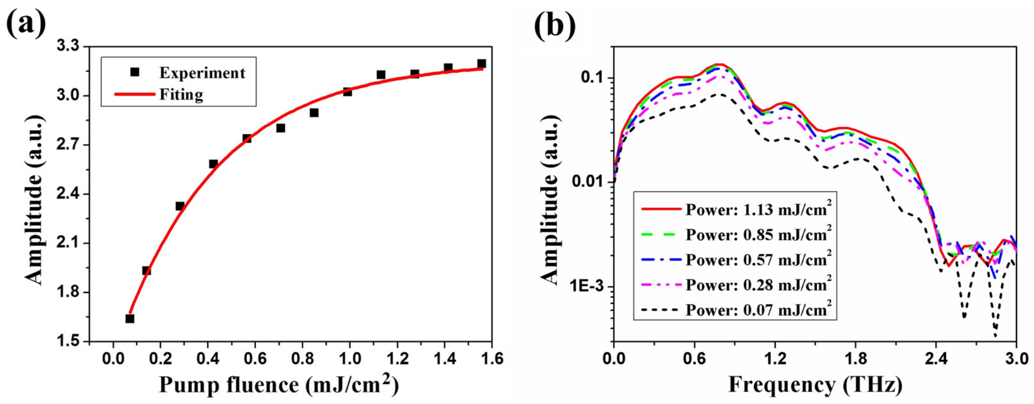

FIG. 4. (a) Pump power dependence of peak-to-peak amplitude of the generated THz radiation from WS_2; (b) Fourier-transformed spectra with the pump power of 0.07, 0.28, 0.57, 0.85, and 1.13 mJ/cm^2.

the E_X component regardless of the incident polarization states. This is the feature of the current-surge effect based on transient current at a semiconductor surface. When an oblique incident laser illuminates on the sample surface, a large amount of photoexcited carriers are accumulated and accelerated along the direction of surface build-in field (normal to the surface), which leads to the in-plane THz radiation that is different than the depolarization of multiferroic materials such as $BiFeO_3$ [37]. Under the excitation by the pump energy (1.55 eV), which is greater than the band gap (1.35 eV) of WS_2, the photogenerated carriers can be accelerated in the surface depletion region by surface built-in field. This field can be formed by either band bending at the surface or the photon-Dember effect due to a mobility difference between electrons and holes, resulting in a transient current along the surface normal. Additionally, the THz E_X amplitude by *P*-polarized excitation is 1.2 times larger than that by *S*-polarized excitation, which is due to the projection of different polarization on the detection plane as discussed by previous work [21].

To confirm the dominant THz generation mechanism of WS_2, the relation between THz radiation amplitude and the pump influence is studied in Fig. 4(a), which shows that peak-to-peak amplitude of the generated THz radiation from WS_2 increases with the increase of the pump influence. When the pump influence approaches 1.13 mJ/cm^2, the THz radiation amplitude is saturated and maintained stable. The relevant Fourier-transformed spectra under the pump of 0.07, 0.28, 0.57, 0.85, and 1.13 mJ/cm^2 are shown in Fig. 4(b). The intensity of THz radiation in frequency domain gradually reaches saturation in the range from 0.3 to 2.4 THz evidently. This pump influence dependence is quite different from that of MoS_2, which demonstrates the dominated optical rectification as the THz radiation presents linear dependence on the ever-increasing pump influence. The main reason for the saturation is due to the abundant photoexcited carriers accumulated at the surface after high intensity excitation, which leads to electrostatic screening of photocarriers [38]. Therefore, the results suggest that the dominant THz generation mechanism is associated with semiconductor surface transient current.

The azimuthal angle dependence [please see the inset of Fig. 3(a)] of THz radiation can be used to distinguish the THz radiation from nonlinear polarization and transient current as shown in Eq. (1). For a comparison, we demonstrate azimuthal angle dependence of THz radiation for both 2*H*-WS_2 and 2*H*-MoS_2. As shown in Fig. 5(a), the THz amplitude of the 2*H*-MoS_2 demonstrates threefold rotation symmetry on the azimuthal angle, which has been analyzed in our previous work [21]. However, the THz radiation from 2*H*-WS_2 is insensitive to the azimuthal angle, which demonstrates a circular response in the polar system as shown in Fig. 5(a). This may suggest that the dominant THz radiation is from the surfing current combined with the data in Fig. 4(a). Is the THz radiation from WS_2 from the surfing current totally? To answer this question, we took the THz radiation as a function of the incident excitation polarized angle by rotating the HWP from 0° to 360° (0° and 90° correspond to *P* polarized and *S* polarized, respectively). Interestingly, Fig. 5(b) demonstrates that THz amplitudes generated by both WS_2 and MoS_2 are sensitive to the incident pump polarization angle and present 2φ relation with the excitation polarized angle. For better understanding the mechanism of THz radiation, we calculated the nonlinear optical coefficient by the first-principle method (see the calculated process and parameters in the Supplemental Material [39]). The effective nonlinear optical coefficient $d_{ij}(i = 1,2,\ldots,6;\ j = 1,2,\ldots,6)$ is obtained. According to the nonlinear polarization components, the THz radiation based on the azimuthal angle can be written as [21]

$$E_{\mathrm{THz}} \propto 0.97[d_{22}\sin(3\varphi) - 2d_{15}] + 0.24(d_{31} + d_{33}), \quad (2)$$

where φ is the azimuthal angle and d_{15},d_{22},d_{31}, and d_{33}, are the effective nonlinear optical coefficients. From the first-principle calculation (Fig. S1 in the Supplemental Material [39]), we can see that d_{22} is quite low at 1.55 eV and the parameters $d_{31} \gg d_{22}$. Thus, Eq. (2) can be simplified as $E_{\mathrm{THz}} \propto 0.24(d_{31} + d_{33}) - 1.94d_{15}$. Besides, the nonlinear optical coefficient d_{ij} of MoS_2 is obtained by first-principle calculation with the corresponding parameters from Ref. [21]. First, the parameter d_{22} of MoS_2 (3.80 pm/V) is larger than that of WS_2 (0.5 pm/V) at 1.55 eV. The difference is mainly caused by the different density of states (DOS), which depends on the interatomic spacing, atomic charge, and crystalline structure of the two materials. Second, the parameter d_{22} of MoS_2 is fifty times larger than other parameters such as d_{15}, d_{33} at 1.55 eV. According to Eq. (2), the THz radiation based on the azimuthal angle reveals that the 3φ dependence on the

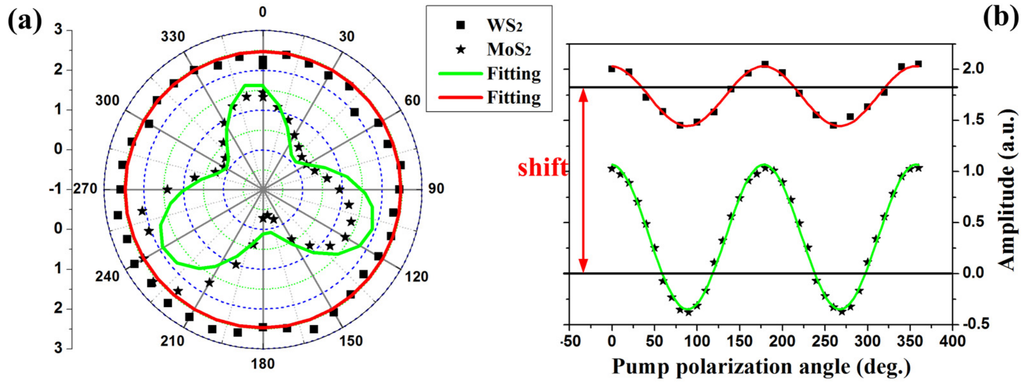

FIG. 5. (a) Azimuthal angle and (b) pump polarization angle dependence of peak-to-peak amplitude of the THz radiation for WS_2 and MoS_2, respectively. Squares and pentagons represent experimental data for WS_2 and MoS_2, respectively, while red and green lines represent the fitting results for WS_2 and MoS_2, respectively.

azimuthal angle is dominated by d_{22}, so MoS_2 demonstrates stronger 3φ dependence on the azimuthal angle than that of WS_2. This suggests that the THz radiation from MoS_2, which is mainly affected by d_{22}, is accompanied by the $\sin(3\varphi)$ term, while the THz radiation from WS_2 can also be relevant to the nonlinear response. Nevertheless, this response comes from the different nonlinear optical coefficients without the threefold rotation symmetry term in the azimuthal dependence expression. Furthermore, after the coordinate transformation based on the polarization angle of the pump beam, the generated THz radiation formula dependence on the incident polarization angle α can be expressed as [21]

$$E_{\mathrm{THz}} \propto A\cos\alpha + B\sin\alpha + C\cos(2\alpha) + D\sin(2\alpha) + E, \tag{3}$$

where A, B, C, D, E are fitting constants, relating to the nonlinear optical coefficients d_{15},d_{22},d_{31}, and d_{33}. 2α dependence on the pump polarization angle [Fig. 5(b)] is dominated by optical rectification, which complies with the Eq. (3). Due to the difference of optical rectification contribution, the amplitude modulation of MoS_2 is larger than that of WS_2. Besides, the amplitude of THz radiation from WS_2 presents a very large shift [Fig. 5(b)] which is generated by the surface depletion field. We can calculate the ratio of nonlinear polarization contribution in the total THz radiation according to the formula $(I_{\max} - I_{\min})/2I_{\max}$ [24]. From Fig. 5(b), the deduced nonlinear polarization contribution (optical rectification) for WS_2 is 12%. Besides, the layered materials WS_2 would have specific dipole orientations for the out-of-plane dipole transition and in-plane dipole transition excited by P and S polarization respectively, which may lead to anisotropic absorption [40]. In our experiment, the THz radiation process occurred in the surface depletion region in WS_2. The anisotropic absorption between P and S polarization in the depletion region is approximately 0.13% (more information, please refer to the Supplemental Material [39]), which is less than the 12% modulation observed in Fig. 5(b). This further suggests that even though WS_2 and MoS_2 have the same crystalline structure and electric structure, they demonstrate quite different THz radiation mechanisms, one mainly based on the optical rectification effect, while the other is mainly based on the surface current-surge effect.

B. THz radiation under transmission configuration

The schematic of incident angle change in the transmission configuration is shown in Fig. 6(a). The angle is mainly limited by the sample holder (polyethylene plate), which can rotate around the center axis in a set of angles. The incident angle θ_1 and output radiated angle θ_2 [Fig. 6(a)] obey approximately a generalized Fresnel law as $n_1\sin(\theta_1) = n_2\sin(\theta_2)$. n_1 and n_2 are the refraction index of the incident optical beam in the air and the THz beam through the sample. The output radiated angle θ_2 is estimated to be 9.3° at the incident angle 45°. When the incident angle θ is 40° and $-40°$, the THz radiated pulses demonstrate polarity reversal [Fig. 6(b)], which is similar to the THz radiation from GaAs. Such a polarity reversal (THz amplitude sign change) is an evidence of photoinduced currents propagating in a direction perpendicular to the surface. No THz emission is detected at normal incidence of the pump beam ($\theta = 0°$), which suggests the nonlinear polarization is trivial. Additionally, Fig. 6(c) demonstrates the azimuthal angle dependence of the THz radiation from WS_2 with fixed incident angle at 5° or 45°. Consistent with the data in Fig. 5(a), the amplitudes of the THz radiation are nearly constant with azimuthal angle of the sample. Besides, the pump polarization angle dependence of THz radiation in the transmission configuration is obtained as shown in Fig. S3 in the Supplemental Material [39]. Similar to the results from the reflection configuration, the THz radiation presents a 2α dependence on the pump polarization angle.

As discussed above, the intrinsic electric field can introduce the dominant THz radiation instead of optical rectification. Is this intrinsic field in WS_2 from the surface state or from the photo-Dember effect? To answer this, we compare the mobility of electrons and holes of WS_2 and InAs. InAs is a traditional narrow band-gap semiconductor, from which the dominant THz radiation is due to the photon-Dember effect. The physical property of InAs and WS_2 are listed in Table I.

From Table I, we can see that the mobility ratio of electrons and holes of InAs outdistance that of WS_2 by two orders. The electron mass and hole mass are almost similar in WS_2, while

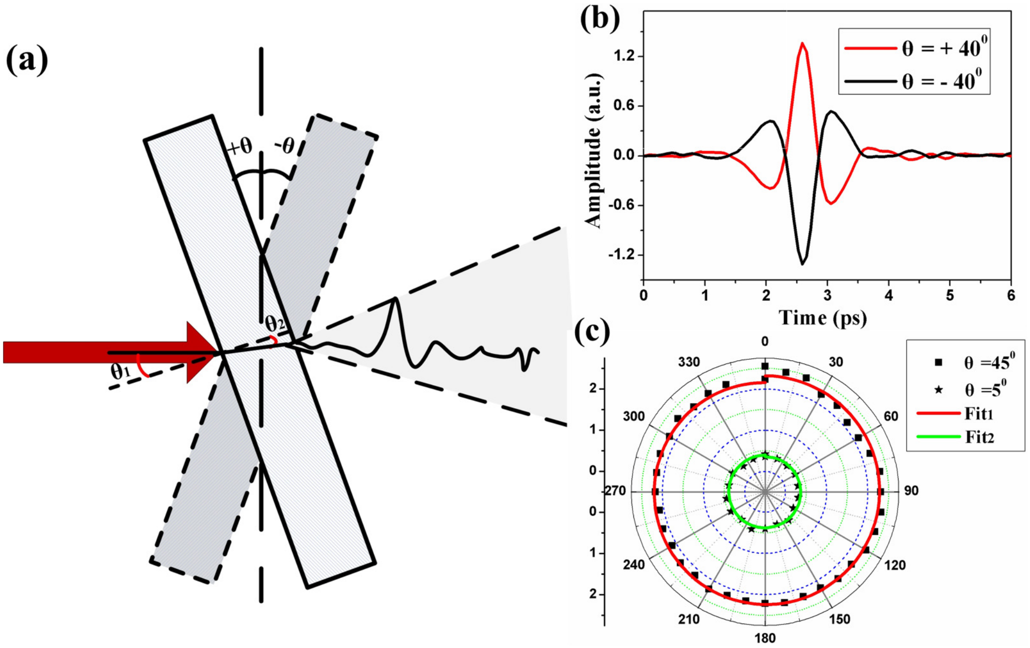

FIG. 6. (a) Schematic of incident angle change; (b) Incident angle dependence of the THz radiation (red for 40°, black for −40°); (c) Azimuthal angle dependence of the THz radiation at the 5° and 45° incident excitation. The experimental and fitting results are depicted with dotted and solid lines, respectively.

the electron mass is one order less than the hole mass in InAs. This implies that the photon-Dember effect cannot be the main effect for THz radiation in WS_2. Thus, the surface of WS_2 can form a strong depletion of electric field similar to the wide band-gap semiconductor GaAs ($Eg = 1.43$ eV) or InP ($Eg = 1.34$ eV). When the optical pulse illuminates the surface of WS_2, it easily generates gradient internal field to accelerate the photocarriers and form transient current, resulting in THz radiation.

C. Angular dependent THz radiation from WS_2

According to the above analysis, the primary THz generation mechanism of the $2H$-WS_2 is due to the photogenerated carriers' acceleration under surface depletion field. This surface depletion field is mainly due to the crystal periodic arrangement breaking on the surface. Unlike the traditional semiconductors such as GaAs, the dangling bond is the main reason for the surface states. However, WS_2 is a layered material with the van der Waals interaction between layers with a much steeper surface potential field than that of traditional semiconductors. For comparison, the THz radiation of both WS_2 and GaAs(100) are obtained under the same experimental conditions (Fig. S4 in the Supplemental Material [39]). The difference of intensity and pulse width mainly result from the different carrier mobility and scattering rate between two materials [37]. To maintain the Fermi level consistent inside and outside the semiconductors, the Fermi-level pinning occurs at the surface, leading both the conduction- and valence-band bending and forming a depletion layer with a width l_d at the surface [Fig. 7(a)], where the intensity of built-in field is affected by barrier potential and doping concentration. Intrinsic WS_2 usually demonstrates p type [43] and the surface depletion field E_d taking place on a semiconductor surface can be expressed as [22]

$$E_d = \frac{eN_D}{\kappa} l_d, \tag{4}$$

where e is the electron charge, N_D is the doping concentration, $\kappa = \varepsilon_r \varepsilon_0$ is the permittivity, $\varepsilon_r = 14.4$ [44],

TABLE I. Physical properties of WS_2 [41] and InAs [42].

Sample	WS_2	InAs
Bang gap (eV)	1.35	0.36
Electron mobility μ_e[cm^2/(V s)]	690	30000
Hole mobility μ_e[cm^2/(V s)]	540	240
Electron mass m_e	$0.31m_e$	$0.027m_e$
Hole mass m_h	$0.42m_e$	$0.33m_e$

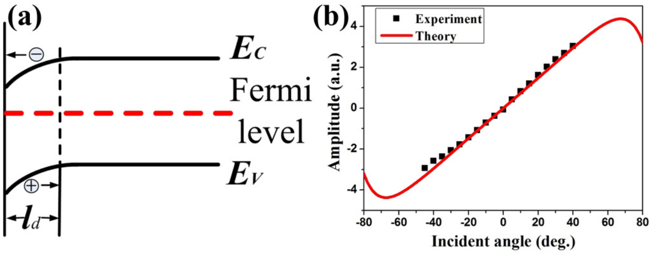

FIG. 7. (a) Surface band diagram of p-type crystal WS_2 in room temperature. Photoexcited carriers are swept to cross the depletion width l_d by the built-in field; (b) incident angle dependent THz radiation in the transmission configuration with experimental data (dots) and theoretical calculation (red curve).

$\varepsilon_0 = 8.85 \times 10^{-14}$ F/cm is the permittivity of vacuum, and $l_d = \sqrt{\frac{2\kappa(V_D - kT/e)}{eN_D}}$. $kT/e = 0.026$ V is the thermal potential under room temperature. V_D is the surface potential barrier, which is approximately 0.58 V for the semiconductor WS_2 with $N_D = 10^{17}/\text{cm}^3$ under room temperature [45]. The maximum value of the surface depletion field could reach as high as 1.2×10^5 V/cm approximately and the depletion width is approximately 94 nm.

The radiated process can be viewed as a dipole oscillation radiation. The intensity of THz radiation can be described by the formula [46]

$$E_{\text{THz}} \propto \frac{\partial N(t)}{\partial t} e\mu E_s \sin(\theta), \tag{5}$$

where the μ is electron mobility, e is the electron charge, $N(t)$ is the density of photoexcited free electrons, and E_S is the intensity of the surface field. The θ represents the incident angle of the pump laser as shown in Fig. 6(a). In the model of Hertzian dipole, Eq. (5) can be further simplified as $E_{\text{THz}} \propto \sin(\theta)$. When the incident pulse is perpendicular to the sample surface ($\theta = 0^\circ$), the amplitude of radiation is near zero in the transmission configuration. With the change of incident angle $\pm\theta$, the polarity of radiated THz is reversed as the THz radiation is an odd function of angle in Eq. (5), which is consistent with the experimental data in Fig. 6(b). This radiation is not related to the polarization of the pump beam. To further verify this, we do the experiments of THz radiation under elliptically polarized excitation as shown in Fig. S5 in the Supplemental Material [39]. Generally, the THz radiation intensity is insensitive to both the left and right elliptically polarized excitations, which suggests that the polarization of pump beam cannot take effect on the THz radiation based on the surface field.

The incident angle dependent THz radiation in the transmission configuration is shown in Fig. 7(b) with experimental data (dots) and theoretical calculation (red curve). The calculation is based on the following formula [22]:

$$E(\theta) \propto \sin(\theta)\left[1 - \left(\frac{\tan(\theta - \theta_2)}{\tan(\theta + \theta_2)}\right)^2\right] \times \frac{2\cos(\theta)\sin(\theta_2)}{\sin(\theta + \theta_2)\cos(\theta - \theta_2)}, \tag{6}$$

where $\theta_2 = \sin^{-1}[\sin\theta/n_2]$ and n_2 is the refractive index of the radiated THz field. The refractive index n_2 is approximately 4.4 at 1 THz by THz time-domain transmission spectroscopy. The calculation agrees well with the experimental data with the Brewster angle at approximately 69.0°. The Brewster angle happens at extreme values of Eq. (6) with $\frac{\partial E(\theta)}{\partial \theta} = 0$. The Brewster angle is proportional to the refractive index as $\theta_B \propto n_2$.

IV. CONCLUSION

In summary, THz radiation and surface characterization have been investigated particularly by THz surface emission spectroscopy under transmission and reflection configuration and reveal that the THz radiation mechanism of crystal WS_2 is dominated by surface field. The results are different from that of MoS_2 based on optical rectification in spite of similar physical structure and optoelectronic properties between them. Due to the screening effect, the radiated THz intensity demonstrated a saturation effect with the incident pump influence up to $1.13\ \text{mJ/cm}^2$. The intensity of THz radiation is insensitive to the azimuthal angle of WS_2, and the contribution of the nonlinear effect is approximately 12%. The results are also confirmed by the nonlinear optical coefficient calculation by the first-principle method. Besides, the surface field characterization of WS_2 crystal is analyzed by the Fresnel law combined with the dipole radiation model. We find the maximum value of the surface depletion field could be as high as approximately 1.2×10^5 V/cm. As few experiments are done in THz region for the layered materials, these optical and physical surface processes are important factors reflecting the light-matter interaction. Particularly, with the rapid development of ultrafast laser and material science, the THz radiation interface response is also a precious asset for optoelectronic and photonic applications of layered materials. Therefore, our results would further pave the way for the THz radiation property studying layered materials and promote the THz applications with layered materials.

ACKNOWLEDGMENTS

This work was supported by National Natural Science Foundation of China (Grants No. 11774288 and No. 11374240) and Natural Science Foundation of Shaanxi Province (Grant No. 2017KCT-01).

---

[1] Y. L. Chen, J. G. Analytis, J. H. Chu, Z. K. Liu, S. K. Mo, X. L. Qi, H. J. Zhang, D. H. Lu, X. Dai, Z. Fang, S. C. Zhang, I. R. Fisher, Z. Hussain, and Z. X. Shen, Science **325**, 178 (2009).

[2] K. S. Novoselov, Z. Jiang, Y. Zhang, S. V. Morozov, H. L. Stormer, U. Zeitler, J. C. Maan, G. S. Boebinger, P. Kim, and A. K. Geim, Science **315**, 1379 (2007).

[3] J. G. Bednorz and K. A. Müller, *Ten Years of Superconductivity: 1980–1990* (Springer, Amsterdam, 1986), p. 267.

[4] T. W. Yoichi Kamihara, M. Hirano, and H. Hosono, J. Am. Chem. Soc. **130**, 3296 (2008).

[5] Y. Tan, R. He, C. Cheng, D. Wang, Y. Chen, and F. Chen, Sci. Rep. **4**, 7523 (2014).

[6] K. F. Mak, C. Lee, J. Hone, J. Shan, and T. F. Heinz, Phys. Rev. Lett. **105**, 136805 (2010).

[7] K. P. Wang, J. Wang, J. T. Fan, M. Lotya, A. O'Neill, D. Fox, Y. Y. Feng, X. Y. Zhang, B. X. Jiang, Q. Z. Zhao, H. Z. Zhang, J. N. Coleman, L. Zhang, and W. J. Blau, ACS Nano **7**, 9260 (2013).

[8] T. Cao, G. Wang, W. Han, H. Ye, C. Zhu, J. Shi, Q. Niu, P. Tan, E. Wang, B. Liu, and J. Feng, Nat. Commun. **3**, 887 (2012).

[9] S. Bikorimana, P. Lama, A. Walser, R. Dorsinville, S. Anghel, A. Mitioglu, A. Micu, and L. Kulyuk, Opt. Express **24**, 20685 (2016).
[10] F. Withers, O. Del Pozo-Zamudio, A. Mishchenko, A. P. Rooney, A. Gholinia, K. Watanabe, T. Taniguchi, S. J. Haigh, A. K. Geim, A. I. Tartakovskii, and K. S. Novoselov, Nat. Mater. **14**, 301 (2015).
[11] M. Tsai, J. Chang, D. Tsai, C. Chen, C. Wu, L. Li, L. Chen, and J. He, ACS Nano **8**, 8317 (2014).
[12] V. Podzorov, M. E. Gershenson, C. Kloc, R. Zeis, and E. Bucher, Appl. Phys. Lett. **84**, 3301 (2004).
[13] A. S. Pawbake, R. G. Waykar, D. J. Late, and S. R. Jadkar, ACS Appl. Mater. Interfaces **8**, 3359 (2016).
[14] N. Kumar, J. He, D. He, Y. Wang, and H. Zhao, J. Appl. Phys. **113**, 133702 (2013).
[15] P. P. Callum, J. Docherty, H. J. Joyce, M.-H. Chiu, C.-H. Chen, M.-Y. Lee, L.-J. Li, L. M. Herz, and M. B. Johnston, ACS Nano **8**, 11147 (2014).
[16] J. F. Federici, B. Schulkin, F. Huang, D. Gary, R. Barat, F. Oliveira, and D. Zimdars, Semicond. Sci. Technol. **20**, 266 (2005).
[17] Y. C. Shen and P. F. Taday, IEEE J. Sel. Top. Quantum Electron. **14**, 407 (2008).
[18] T. Nagatsuma, S. Horiguchi, Y. Minamikata, Y. Yoshimizu, S. Hisatake, S. Kuwano, N. Yoshimoto, J. Terada, and H. Takahashi, Opt. Express **21**, 23736 (2013).
[19] X. Y. Deng, X. H. Deng, F. H. Su, N. H. Liu, and J. T. Liu, J. Appl. Phys. **118**, 224304 (2015).
[20] X. Yan, L. Zhu, Y. Zhou, Y. E. L. Wang, and X. Xu, Appl. Opt. **54**, 6732 (2015).
[21] Y. Huang, L. Zhu, Q. Zhao, Y. Guo, Z. Ren, J. Bai, and X. Xu, ACS Appl. Mater. Interfaces **9**, 4956 (2017).
[22] X. C. Zhang and D. H. Auston, J. Appl. Phys. **71**, 326 (1992).
[23] X. Wu, X. Xu, X. Lu, and L. Wang, Appl. Surf. Sci. **279**, 92 (2013).
[24] P. Gu, M. Tani, S. Kono, K. Sakai, and X. C. Zhang, J. Appl. Phys. **91**, 5533 (2002).
[25] L. V. Titova, C. L. Pint, Q. Zhang, R. H. Hauge, J. Kono, and F. A. Hegmann, Nano Lett. **15**, 3267 (2015).
[26] Q. H. Wang, K. Kalantar-Zadeh, A. Kis, J. N. Coleman, and M. S. Strano, Nat. Nanotechnol. **7**, 699 (2012).
[27] J.-W. Chung, Z. R. Dai, and F. S. Ohuchi, J. Cryst. Growth **186**, 137 (1998).
[28] T. Sekine, K. Toyoda, K. Uchinokura, and E. Matsuura, Solid State Commun. **35**, 371 (1980).
[29] A. Rice, Y. Jin, X. F. Ma, X. C. Zhang, D. Bliss, J. Larkin, and M. Alexander, Appl. Phys. Lett. **64**, 1324 (1994).
[30] J. Hebling, A. G. Stepanov, G. Almaasi, B. Bartal, and J. Kuhl, Appl. Phys. B **78**, 593 (2004).
[31] H. Kurosawa, T. Ishihara, N. Ikeda, D. Tsuya, M. Ochiai, and Y. Sugimoto, Opt. Lett. **37**, 2793 (2012).
[32] M. B. Johnston, D. M. Whittaker, A. Corchia, A. G. Davies, and E. H. Linfield, Phys. Rev. B **65**, 165301 (2002).
[33] R. Kersting, J. N. Heyman, G. Strasser, and K. Unterrainer, Phys. Rev. B **58**, 4553 (1998).
[34] L. G. Zhu, B. Kubera, K. Fai Mak, and J. Shan, Sci. Rep. **5**, 10308 (2015).
[35] M. E. Barnes, S. A. Berry, P. Gow, D. McBryde, G. J. Daniell, H. E. Beere, D. A. Ritchie, and V. Apostolopoulos, Opt. Express **21**, 16263 (2013).
[36] V. Apostolopoulos and M. E. Barnes, J. Phys. D: Appl. Phys. **47**, 374002 (2014).
[37] K. Takahashi, N. Kida, and M. Tonouchi, Phys. Rev. Lett. **96**, 117402 (2006).
[38] X. Wu, B. Quan, X. Xu, F. Hu, X. Lu, C. Gu, and L. Wang, Appl. Surf. Sci. **285**, 853 (2013).
[39] See Supplemental Material at http://link.aps.org/supplemental/10.1103/PhysRevB.96.155202 for discussion about the simulation calculation about the nonlinear optical coefficient $d_{ij}(i = 1,2,\dots,6; j = 1,2,\dots,6)$, pump angle dependence of THz radiation in the transmission configuration, anisotropic absorption excited by P and S polarization, THz radiation comparison between WS_2 and GaAs(100), and the dependence of THz generation with the elliptically polarized excitation.
[40] J. A. Schuller, S. Karaveli, T. Schiros, K. He, S. Yang, L. Kymissis, J. Shan, and R. Zia, Nat. Nanotechnol. **8**, 271 (2013).
[41] Z. Jin, X. Li, J. T. Mullen, and K. W. Kim, Phys. Rev. B **90**, 045422 (2014).
[42] P. Gu and M. Tani, in *Terahertz Optoelectronics*, edited by K. Sakai (Springer, Berlin, 2005), p. 63.
[43] N. K. Agarwal, K. Nagireddy, and P. D. Patel, Cryst. Res. Technol. **15**, 65 (1980).
[44] J. Cazaux, Opt. Commun. **3**, 221 (1971).
[45] C. Ballif, M. Regula, and F. Lévy, Sol. Energy Mater. Sol. Cells **57**, 189 (1999).
[46] X. C. Zhang, B. B. Hu, J. T. Darrow, and D. H. Auston, Appl. Phys. Lett. **56**, 1011 (1990).